International Journal of Rock Mechanics & Mining Sciences 157 (2022) 105167



Contents lists available at ScienceDirect

International Journal of Rock Mechanics and Mining Sciences

journal homepage: www.elsevier.com/locate/ijrmms





Determining Young's modulus of granite using accurate grain-based modeling with microscale rock mechanical experiments

Xuhai Tang [a], Yiheng Zhang [a], Jingjing Xu [a,*], Jonny Rutqvist [b], Mengsu Hu [b], Zhengzhi Wang [a], Quansheng Liu [a]

[a] School of Civil Engineering, Wuhan University, Wuhan, 430072, Hubei, China
[b] Lawrence Berkeley National Laboratory, Berkeley, CA, 94720, USA

ARTICLE INFO

Keywords:
microscale Rock mechanics experiment
Digital rock
Accurate grain-based modeling
Mineralogy
Interphase
Natural granite

ABSTRACT

It is critical to rigorously determine the mechanical properties of granitic rocks to effectively analyze and manage subsurface engineering activities, such as geothermal energy exploitation and nuclear waste disposal. However, the required deep drilling and sampling for macroscale rock mechanics experiments (macro-RME) are challenging and expensive. In this study, we developed a novel accurate grain-based modeling (AGBM) using the results of microscale rock mechanics experiments (micro-RME) to determine the elastic properties of arbitrarily shaped granite. The microstructure of each sample and Young's modulus of rock-forming minerals were measured with a TESCAN Integrated Mineral Analyzer (TIMA) and nanoindentation test. The geometry and Young's modulus of interphases between different minerals were determined using an advanced algorithm with atomic force microscopy (AFM) test. With the microstructure and microscale mechanical properties obtained from the micro-RME, the AGBM was applied to derive the macroscale mechanical properties of the granite samples. This new methodology was demonstrated on small test specimens extracted from granite fragments. Because we can use test specimens from arbitrarily shaped and small rock fragments, this new methodology has been proven to be a breakthrough from the conventional technology of macro-RME.

1. Introduction

Granitic rock formations are commonly associated with hot dry rock (HDR) reservoirs for the exploitation of geothermal energy and are considered for hosting geologic nuclear waste repositories. An important part of site investigation and design is the accurate measurement of mechanical properties. Conventionally, the mechanical properties of rocks are measured by macroscale rock mechanics experiments (macro-RMEs) including uniaxial/triaxial compression tests suggested by the International Society for Rock Mechanics (ISRM) and the American Society for Testing and Materials (ASTM).[1] The rock samples are usually standard cylinders 100 mm in height and 50 mm in diameter, and were prepared from available intact sections of the core. Drilling and recovery of such rock samples in deep reservoirs are expensive and time-consuming and suffer from technical difficulties. Due to high in situ stress, cores achieved by drilling are frequently fragmented,[2] especially core disking, which can occur during deep underground drilling. The host rock around faults is usually highly fractured in a damage zone with a core of fragmented rocks in clay gouge.[3] Thus, significant challenges and limitations exist in conventional rock mechanical testing for any site investigation.

Based on the elastic wave of minerals,[4] the elastic modulus of rock can be evaluated by the Voigt-Reuss-Hill average algorithm,[5] which is widely used to understand the lithology of deep earth formations. The Voigt (upper) and Reuss (lower) bounds are the averaged elastic properties of a polyphase and polycrystalline aggregate assuming homogeneous strain or stress, respectively. The average value provides a convenient estimation for the properties of an aggregate rock without a preferred orientation and with grains locked together.[6] However, the Voigt-Reuss-Hill average algorithm oversimplifies the variability of rocks because it ignores the grain interactions and grain shapes. This causes the elastic properties to scatter widely between the upper and lower theoretical bounds.[7] Further mean-field homogenization schemes have been developed that consider the inclusion geometries based on the Eshelby solution[8] of the ellipsoidal inhomogeneity embedded in an infinite medium. These approaches include the dilute scheme,[9]

* Corresponding author.
E-mail address: xujingjing@whu.edu.cn (J. Xu).

https://doi.org/10.1016/j.ijrmms.2022.105167
Received 10 January 2022; Received in revised form 25 April 2022; Accepted 11 July 2022
Available online 18 July 2022
1365-1609/© 2022 Elsevier Ltd. All rights reserved.

self-consistent approximation,[10] differential scheme,[11] and Mori-Tanaka approach.[12] Unfortunately, none of these analytical models can describe the complex microstructure well and accurately determine the elastic parameters of crystalline rocks. The microstructure (e.g., interphases, pores, and grain geometry) of rocks plays a dominant role in their mechanical response and affects the applicability of these homogenization methods.[13]

To overcome the aforementioned challenges and limitations of core-scale experiments (macro-RME) and analytical homogenization methods, microscale rock mechanics experiments (micro-RME) have been developed to determine rock mechanical properties. First, the technology of micro-RME can test the mechanical properties of specimens that can be quite small and arbitrarily shaped, thus overcoming the difficulties in obtaining core samples for conventional macro-RME. Second, highly heterogeneous and anisotropic properties can be evaluated through their dependency on the distribution of microscale properties. With these advantages, micro-RME technology provides a viable cost-effective approach to testing the mechanical properties of rock samples related to any subsurface science and engineering project.

Nanoindentation test recently attracted great interest in the area of rock engineering.[14] Bobko et al.[15] investigated the mechanical stiffness, anisotropy, and strength properties of shale using nanoindentation tests. Akono et al.[16] investigated sandstone in CO_2-saturated brine and used the statistical nanoindentation method to determine the relationship between the mineral compositional changes at the microscale and the constitutive behavior at the macroscale. Zeng et al.[17] proposed an improved energy-based model to determine the fracture energy and toughness of shale. Based on a continuous stiffness model and big data statistical nanoindentation tests, Zhang and his coworkers developed an analytical method for measuring the cross-scale mechanical properties of rocks,[13,18] which has been successfully used to investigate the water softening properties of shale.[19] Xu et al.[20] investigated the influence of water softening on the elastic and failure properties of shale obtained from weak interlayers of a rock slope. Using numerical models, the results of nanoindentation tests were successfully applied to model the failure process of slopes with weak shale interlayers. Voltolini et al.[21] visualized the indentation of samples as a function of axial load by using X-ray imaging. Then, a series of 3D datasets were used to analyze local strain fields, which provided a unique opportunity to characterize the mechanical properties for predicting proppant and fracture closure evolution.

Atomic force microscopy (AFM) has been widely used to characterize the nanomechanical properties of biological materials[22] but has only recently been applied to cement[23] and natural rocks.[24–26] Liu et al.[27] demonstrated that AFM is a robust and quantitative method to investigate the mechanical properties of shale, which can be considered a nanocomposite material. Graham et al.[28] investigated the mechanical response of calcareous shales over length scales from 10 nm to 100 μm by combining AFM and nanoindentation test. This combination allowed for the consideration of microcracks and achieved a better prediction of Young's modulus.

In recent decades, numerical techniques have been commonly used to help understand complicated mechanisms from a grain-scale perspective.[29,30] Some researchers investigated the relationship between microscale and macroscale properties using traditional grain-based modeling (GBM).[31–33] In conventional GBM, some microscale mechanical properties are measured by micro-RME directly, and the method of numerical calibration with macro-RME results is typically used to roughly estimate other properties that are difficult to measure experimentally. Without extensive data on the microstructure, the geometry of rock-forming minerals is usually simplified using Voronoi meshes based on the statistical grain size distribution. As shown in Table 1, Peng et al.[34] investigated the mechanical behavior of Bukit Timah granites using GBM. The microstructure was represented using a Voronoi mesh, and the microscale mechanical properties were back-calculated by PFC2D numerical calibration against macro-RME results. With GBM, Peng et al.[32] revealed that when confining pressure increases gradually during compression tests, shear cracks along grain boundaries occur while the failure mode changes from splitting to shear. Zhou et al.[35] developed a three-dimensional (3D) GBM with Voronoi gridding in which the microscale mechanical properties were estimated using numerical calibration.

Table 1
Parameters used in references for microscale modeling of granites.

References	Geometry of minerals	Young's modulus of minerals (GPa)	Test methods
37,38	Real microstructure	Biotite: $E_B = 17.21$	Nanoindentation
39	Voronoi mesh	Quartz: $E_Q = 56.37$ Feldspar: $E_F = 83.09$	
35		Biotite: $E_B = 12$	Numerical calibration
32,34		Quartz: $E_Q = 32$ K-feldspar: $E_{KF} = 20$ Plagioclase: $E_P = 26$	
31,33		Biotite: $E_B = 33.8$	Wave velocity
		Quartz: $E_Q = 94.5$ K-feldspar: $E_{KF} = 69.8$ Plagioclase: $E_P = 88.1$	

With micro-RME, more accurate microstructure and microscale mechanical properties of crystalline rocks can be evaluated. Characteristic microstructures derived from digital images are taken into account within the field of digital rock physics to analyze rock mechanical properties.[36] In a study by Mahabadi et al.,[37] the Young's modulus and failure properties of rock-forming minerals were obtained by nanoindentation tests, while the microstructure was obtained using computerized tomography (CT) scanning. With micro-REM and finite-discrete element method (FDEM) modeling, Mahabadi et al.[38] found that microscale heterogeneity of mechanical properties and microcracks at the grain scale can lead to a significant variation in stress distribution and local tensile stress. Meanwhile, oriented biotite flakes and microcracks have a significant impact on fracture propagation. In Abdelaziz et al.,[39] the microstructure was also represented using Voronoi meshing, while the microscale elastic property was extracted from previous micro-RME results,[37] and the microscale failure properties were estimated using numerical calibration. They demonstrated that the path of the macroscopic failure plane is the result of combining local stress conditions with the microstructure of the model. However, the interphases between different rock-forming minerals were ignored in previous work because the sizes of interphases are too small to be measured.

The goal of this work is to measure the entire microstructure and all microscale mechanical properties experimentally and apply those in accurate grain-based modeling (AGBM) to derive the Young's modulus of granite samples. The mineral composition and microstructure of the granite samples were measured using a TESCAN Integrated Mineral Analyzer (TIMA). The mechanical properties of rock-forming minerals and interphases were measured using nanoindentation and AFM, respectively. Finally, the AGBMs were generated based on micro-RME, and microscale simulations of uniaxial compression tests were carried out to determine the macroscale Young's modulus of the granites.

2. Determining macroscale mechanical properties of granites using micro-RME and upscaling modeling

The micro-RME system includes optical microscopy, nanoindentation, TIMA, and AFM. (1) An orthogonal polarization optical microscopy was used to observe the microstructures of mineral morphology, cleavage cracks within mineral grains, bedding, and micropores. (2) The identification and distribution of minerals was investigated by TIMA, which is an automated quantitative analysis system that can identify minerals quickly and accurately. (3) Nanoindentation

was applied to measure the elastic properties of minerals based on the theories of contact mechanics. (4) AFM (Dimension Icon) can extract mechanical properties at a nanoscale resolution owing to the small diameter (10–30 nm) of the probe.[28] Combining it with continuum mechanics models[40] makes it possible to measure the mechanical properties of the interphase between different minerals. Finally, to determine the macroscale mechanical properties of granites using small and arbitrarily shaped rock specimens, AGBM was developed based on the results of micro-RME. As shown in Fig. 1, the basic idea of the present methodology follows three steps.

3. Methodology

3.1. Principles of TIMA test

TIMA identifies rock-forming minerals based on scanning electron microscopy (SEM) in backscattered electron (BSE) imaging modes and energy-dispersive spectroscopy (EDS).[41] The TIMA dot mapping mode imposes a BSE grid with a specific resolution (determined as pixel spacing) over the entire sample. The maximum accuracy of TIMA is 0.2 μm, which can also be used to analyze a variety of geomaterials such as clay minerals (<2 μm) and complex soil particles.[42] Considering the large mineral crystals of granites, in the present work, TIMA collected BSE signals at a pixel spacing of 3 μm (as shown by the black points in Fig. 2) and EDS signals (X-ray spectrum) (>1000 counts) at a pixel spacing of 9 μm (represented by the red points in Fig. 2). Note that some extra EDS signals are collected at the center of minerals to ensure that there is more than one EDS signal in every mineral zone. The millions of energy spectrum test points from zones of similar BSE and EDS signals are carried out on the statistics and fitting calculation to produce single higher quality spectra for each phase (see Fig. 2a–c). The TIMA software automatically distinguishes different phases based on the energy spectrum images. Then, rock-forming minerals are accurately identified by matching the measured energy spectrum images with the mineral standards library. Finally, the geometry and distribution of different rock-forming minerals including biotite, feldspar, and quartz can be displayed by different colors.

3.2. Principles of nanoindentation test

Nanoindentation works by applying a load on a diamond tip to make a small indentation on the surface of the material. Oliver and Pharr developed the theoretical basis of nanoindentation test to measure the Young's modulus of materials.[43,44] To test highly heterogeneous and multiphase materials, grid indentation and statistical methods have been proposed to probe the mechanical properties from a large number of nanoindentations.[45]

The load-depth curve of nanoindentation is used to analyze the mechanical properties of the material. The initial unloading slope (also called contact stiffness S) can be achieved by the elastic solution relating to the applied loading force P and indentation depth h: $S = \frac{dP}{dh}|h = h_{\max}$, where $h_{\max}$ is the maximum indentation depth. The reduced modulus E_r is calculated as[46]

$$E_r = \frac{\sqrt{\pi}}{2\beta\sqrt{A_c}}S \tag{1}$$

where β is a dimensionless correction factor associated with the indenter tip shape. A_c is the projected contact area of the indenter on the sample surfaces, which is typically determined by a function of the maximum contact depth, and h_c: $A_c = f(h_c)$. The contact depth h_c is calculated as $h_c = h_{\max} - \varepsilon\frac{P}{S}$ (ε is a constant that depends on the indenter tip). Then, Young's modulus of the sample is calculated by the following equation:

$$E_{\text{nano}} = \left(1 - \nu_{\text{nano}}^2\right)\left[\frac{1}{E_r} - \frac{1-\nu_i^2}{E_i}\right]^{-1} \tag{2}$$

where ν_{nano} and ν_i are Poisson's ratios of the sample and indenter, respectively. E_i is the Young's modulus value of the indenter, which is

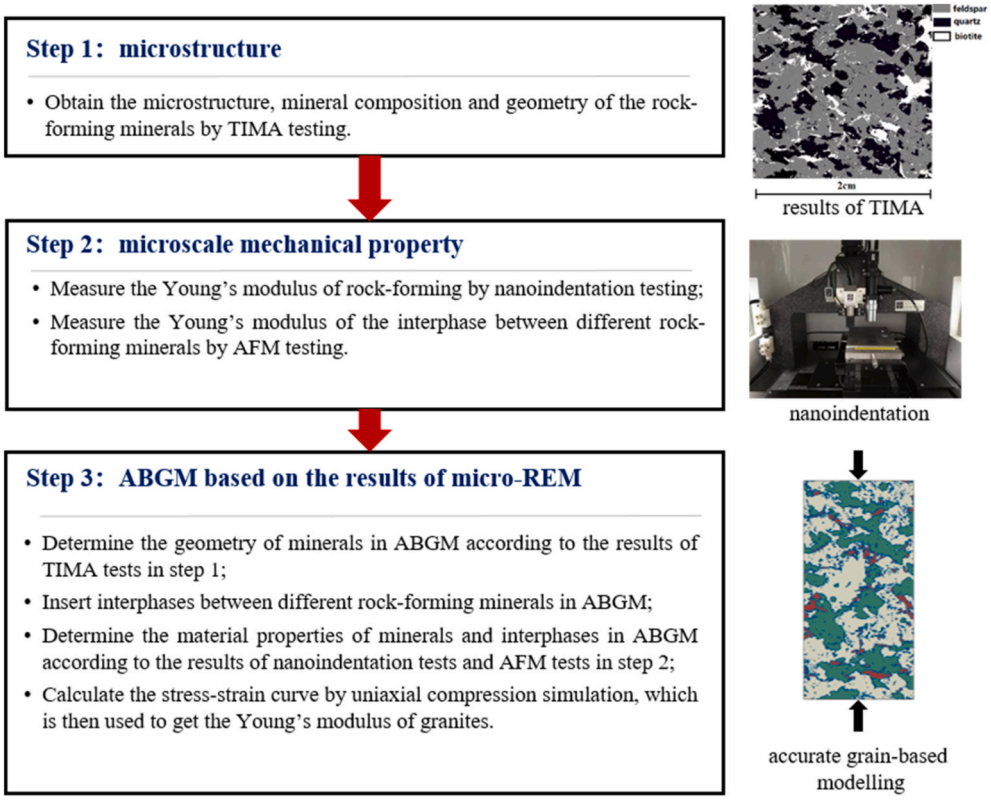


Fig. 1. Flowchart for measuring mechanical properties of small and arbitrarily shaped rock samples using AGBM with micro-RME.

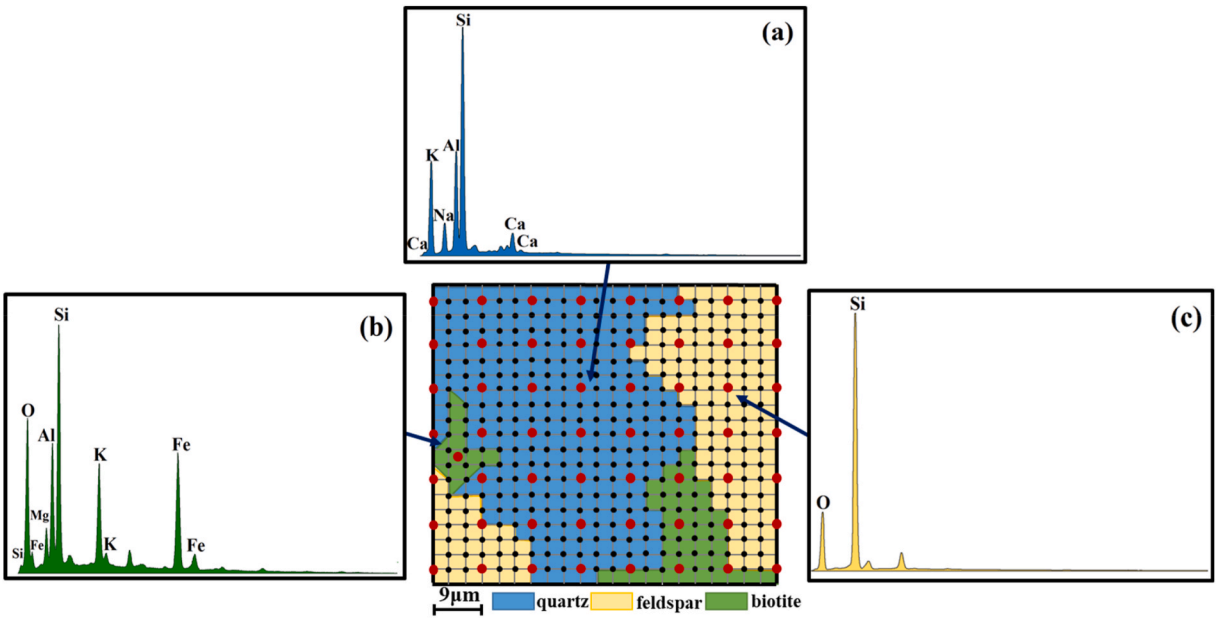


Fig. 2. Different minerals are identified by energy-dispersive spectroscopy in TIMA.

1140 GPa.

3.3. Principals of AFM test

The PeakForce Tapping Mode of AFM was used to produce height images and quantitative nanomechanical maps simultaneously around the interphases between different rock-forming minerals. In this mode, AFM directly measures the interactive force as the tip approaches the surface and retracts from it by recording the cantilever deflection through the laser.[28] Fig. 3 illustrates the force responses corresponding to tip/surface interactions as a function of distance in the approach and retraction stages. In stage 1, the cantilever does not deflect, and there is no interaction force. In stage 2, once the tip reaches the vicinity of the surface, van der Waals (vdW) attraction forces bend the cantilever toward the surface. At stage 3, the tip enters the repulsive contact regime where force increases until the preset maximum force is reached. In stage 4, the tip is retracted. In stage 5, the tip usually stays in contact with the sample after the zero force has passed because of adhesion, resulting in a hysteresis loop. In stage 6, the tip detaches from the surface due to vertical movement in which the force interaction returns to the

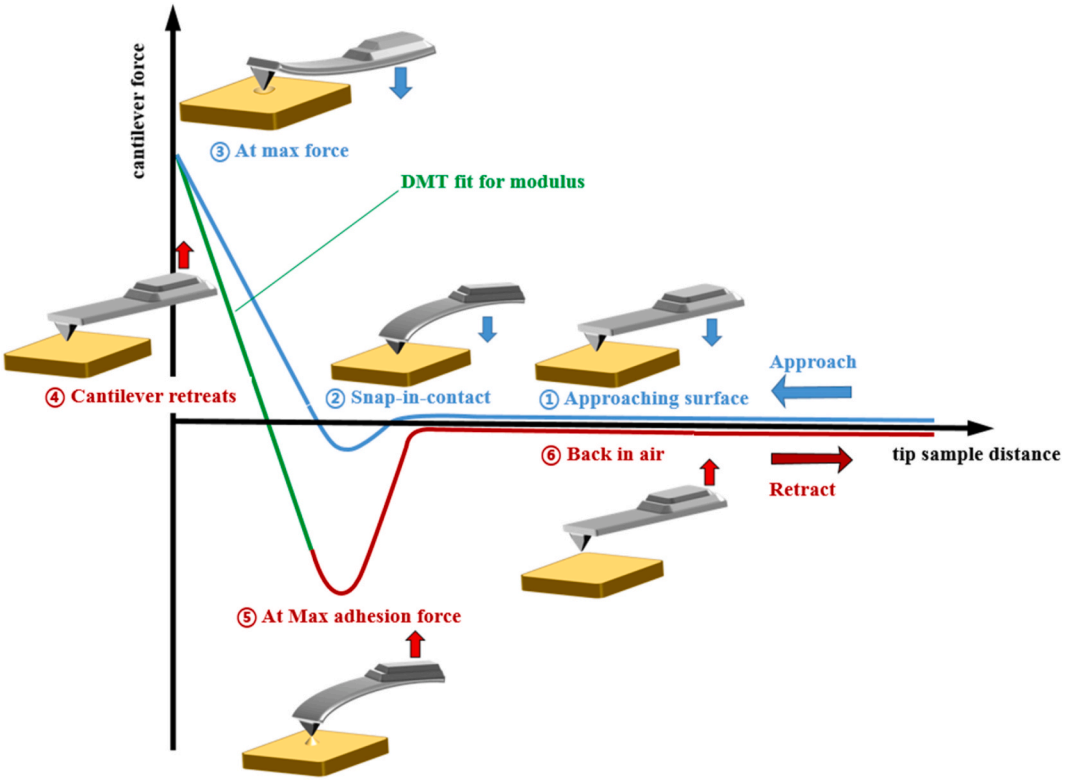


Fig. 3. Corresponding symbolic force curve in each scanning period.

initial no-interaction phase.

A constant peak force is applied to scan the surface of the samples, and the deflection of the cantilevers is measured. In stage 4, the curves between the maximum force and the maximum adhesion are used to fit the contact model by the Dejaguin Muller Toporov (DMT).[40] The reduced Young's modulus $E^{'}$ is given by

$$F = \frac{4E^{'}\sqrt{R(d-d_0)^3}}{3} + F_{\mathrm{adh}} \tag{3}$$

where F is the force acting on the tip, R is the radius of the probe tip, and (d-d_0) is the tip-sample separation distance. F_{adh} is the adhesion force. The reduced Young's modulus $E^{'}$ can be converted to absolute Young's modulus E_{AFM} by the following equation:

$$E^{'} = \frac{1}{\frac{1-\nu_{\mathrm{AFM}}^2}{E_{\mathrm{AFM}}} + \frac{1-\nu_a^2}{E_a}} \tag{4}$$

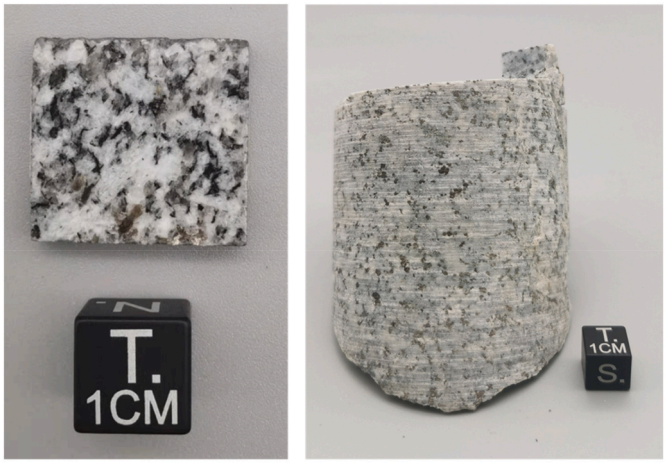
where ν_{AFM} is the Poisson's ratio of the sample, ν_a is the Poisson's ratio of the probe, and E_a is the Young's modulus of the probe.

4. Experimental process

4.1. Preparation of rock specimens

In this work, granitic rock specimens, identified as Bukit Timah granite, were collected in the Mandai area of the central part of Singapore. This granite is a light gray, coarse-granied granodiorite. The macroscale properties of Bukit Timah granites have been investigated by many researchers.[47–49] The macroscale mechanical properties of Bukit Timah granites are strongly heterogeneous, and they are significantly influenced by their rock-forming minerals.[50]

As shown in Fig. 4b, the granites taken from the field can be fragmented and arbitrarily shaped. Then, these granite fragments were cut into cubic specimens with dimensions of 20 mm × 20 mm × 5 mm (Fig. 4a). The surface of each granite specimen was polished in a polisher (Ecomet 250 Buehler) with silicon carbide (SiC) papers of different grain fineness levels including P800, P1200, P2500, and P5000. Before conducting a nanoindentation test, the granite specimens were further polished using an extra fine alumina suspension to reduce the surface roughness as much as possible. This extrafine alumina suspension consists of a diamond suspension (particle size of 0.1, 0.03 μm) and a mixture of ethanol and ethylene glycol at a 1:1 volumetric ratio. Meanwhile, the surfaces of the specimens were cleaned ultrasonically and examined using an optical microscope after each polishing step. The preparation steps mentioned above were carefully conducted to avoid the generation of microcracks within the interfaces as much as possible.



(a) (b)

Fig. 4. (a) Experiment specimens for nanoindentation and AFM tests are prepared from (b) small and arbitrary-shaped pieces of Bukit Timah granite.

4.2. Setting parameters of nanoindentation test

The nanoindentation test was performed on a Hysitron TI950 TriboIndenter system (Hysitron, Inc., Minneapolis, MN, USA). The Berkovich indenter was used for both the indentation tests and in situ scanning probe microscopy (SPM) imaging. The location of each indent was carefully selected under a high-resolution optical microscope to avoid noticeably rough areas. The parameters of grid nanoindentation are listed in Table 2. These were used for quartz, feldspar, and biotite in the following sections. During the loading process of each indentation, (1) the load force was increased linearly to a maximum load of 4 mN at a constant loading rate of 0.8 mN/s (2) The load was held constant for 2 s to reduce the effect induced by thermal drift of the instrument and creep deformation. (3) The load force decreased linearly at a rate of 0.8 mN/s. A total of 4 matrices of indents were conducted on each mineral with each matrix containing a 5 × 5 square grid. The space between two adjacent indents was 10 μm to avoid negative interference. In total, 4 matrices were randomly chosen for each grain at different areas. This approach has been widely used in nanoindentation test to overcome the heterogeneity of minerals.[13,19] The present method is also able to consider the influence of the anisotropy of minerals, such as slices of minerals at different angles.

4.3. Setting parameters of AFM test

Dimension Icon (Bruker Nano/Veeco, Inc., CA) AFM with a Nanoscope V controller and Nanoscope software was employed to obtain both force-displacement curves and surface topographic maps. An optical microscope was used to characterize the minerals and identify relatively flat surfaces. Before each test, the sensitivity of the AFM photodetector (deflection sensitivity) was measured using a clean sapphire standard.[27] Quartz was used to calibrate the radius of the probes. We chose the DNISP-HS probe, which is sufficiently stiff to avoid significant deformation of the probe itself, so it is optimal for measuring materials with Young's modulus ranging from 0 to 100 GPa. After calibration, a scan of 60 μm × 60 μm was carried out at a resolution of 256 × 256 pixels at 0.2 Hz for the granitic samples.

5. Experimental results

5.1. Mineral composition and microstructure of granitic samples

The present experiment took only 1.5 h by TIMA to test a 20 × 20-mm granite specimen, which was completed at the Chengpu geological Testing Co., Ltd, Langfang, China. Then, in grayscale images, the biotite, feldspar, and quartz were presented as white, gray and black, respectively, as shown in Fig. 5. With grayscale images, the mineralogical composition, mineral size, and mineral distribution can be analyzed easily by computers. This Bukit Timah granite consists of quartz (SiO_2, volume approx. 30.40%) and feldspars [including potassium feldspar ($K_{0.91\text{-}0.96}$ $Al_{0.97\text{-}1}Si_{2.98\text{-}3.03}O_8$) and sodium feldspar ($Na_{0.82\text{-}1.04}Al_{0.97\text{-}$

Table 2
Parameters of each indentation and grid nanoindentation.

Item	Value
Loading rate of each indentation	0.8 mN/s
Unloading rate of each indentation	0.8 mN/s
Holding period of each indentation	2 s
Maximum load force of each indentation	4 mN
Indentation grid	5 × 5 square grid
Matrix	4
Spacing between two adjacent indentations	10 μm

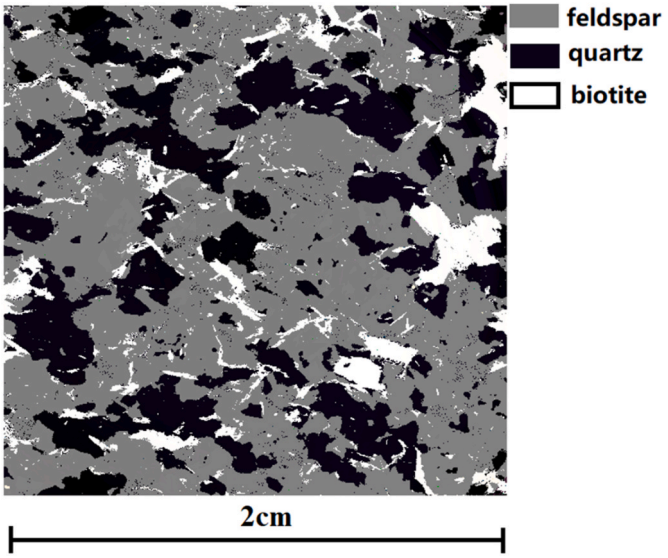


Fig. 5. Mineral composition map of Bukit Timah granite.

$_{0.99}Si_{3.01\text{-}3.07}O_8$), volume approx. 57.74%] in addition to minor amounts of biotite [$(Mg,Fe)_3(Si,Al)_4O_{10}(OH)_2$ $(Mg,Fe)_3(OH)_6$, volume approx. 11.42%].

As shown in Fig. 5, the sizes of quartz, feldspar, and biotite grains are over 1 mm. Therefore, the elastic property of these rock-forming minerals can be measured using a nanoindentation test, which is able to assess mechanical properties at length scales of 500 nm–3000 nm. The Bukit Timah granite is a compact crystalline rock, and the interphases between different minerals are nearly invisible. Moreover, the intercrystalline region is highly porous, especially at the scale of the nanoindenter tip, so it is difficult to isolate the mechanical response of the interphase by nanoindentation since the elastic response is heavily influenced by porosity.[39] The resolution of AFM test is much higher than that of nanoindentation test. Therefore, AFM test can be applied to measure the geometry and mechanical properties of interphases between different minerals.

5.2. Elastic property of rock-forming minerals

5.2.1. Quartz

The quartz was identified based on perpendicularly polarized light images from thin section observations (see Fig. 6a). The typical load-depth curves of quartz are shown in Fig. 6b. Some typical residual indents on the quartz surface obtained by in situ SPM imaging are shown in Fig. 6c–d. Several characteristics can be found: (1) The maximum penetration depth of quartz reaches 150 nm, which satisfies the scale separation criterion and the assumption of a continuum indentation model of an infinite half-space. (2) The load-depth curves of quartz are smooth (see Fig. 6b). (3) Because of the high purity and extremely low surface roughness of quartz (see Fig. 6d), the 100 load-depth curves approximately coincide (see Fig. 6b), which indicates the spatial homogeneity of quartz. (4) Because the quartz is extremely hard and stiff, the depth of the residual indents on a quartz particle is small (see Fig. 6c). (5) To demonstrate for better display, an experimental frequency plot for of Young's modulus is represented in Fig. 6e, which was fitted by probability density functions (PDF). The Young's modulus of quartz is 96.81 GPa. The measured value is consistent with the values measured by nanoindentation and wave velocity in Refs. 51,52. Additionally, the standard deviation for calculating Young's modulus is 1.01 GPa, which indicates that the discrete values tend to be close to the achieved value (expected value).

5.2.2. Feldspar

Fig. 7 shows a set of thin section observation image, load-depth curves, residual indents, and experimental histogram of nanoindentation on feldspar. There are a few features that are worth noting: (1) The maximum penetration depth of feldspar reaches 350 nm. (2) The curves of feldspar are relatively smooth (see Fig. 7b). (3) The relatively large surface roughness of feldspar (see Fig. 7d) and different types of feldspar (including albite, K-feldspar, and anorthite) result in discrete load-depth curves (see Fig. 7b). (4) The residual indent on feldspar indicates a larger penetration depth than that of quartz (see Fig. 7c). (5) The experimental frequency plot of Young's modulus is represented in Fig. 7e. The PDF deconvolutions intuitively recognized three mechanically distinct phases in the feldspar. The peak values of the three fitting curves are E_1 = 64.42 GPa, E_2 = 69.54 GPa, and E_3 = 76.25 GPa, respectively. Despite the fact that there are different mechanical phases in feldspar, their Young's modulus values are very similar. Therefore, they were grouped together into one composite phase, which was used in the following AGBM. The Young's modulus of feldspar was calculated by $E = v_1E_1+v_2E_2+v_3E_3$ (v_1 = 0.2610, v_2 = 0.5169, and v_3 = 0.2221 are volumetric fractions of individual phases), and its value is 69.50 GPa.

5.2.3. Biotite

A thin section observation image, typical load-depth curves, experimental histogram, and residual indents of nanoindentation are shown in Fig. 8 to characterize the microstructure and mechanical properties of biotite. Several characterizations are further discussed: (1) The maximum penetration depth of biotite reaches 550 nm. (2) The loading stages of these curves are not smooth, and steps exist in almost every curve. A striking feature common to nearly all curves is the presence of multiple, randomly occurring pop-ins or discontinuities of varying extensions in the loading segments (see Fig. 8c). (3) The loading segments of the curves prior to the occurrence of relatively larger pop-ins are consistent and overlap with each other. That is, dispersion of the curves commences after pop-ins take place (see Fig. 8c). (4) Three radial cracks are observed to emanate from the three corners of the residual indent (see Fig. 8e). As the indenter penetrates deeper into the biotite, the delaminated layers are forced to curve up until bending failure occurs. The cleavage of biotite results in abrupt cracking and layer delamination under the indenter, which are reflected as discontinuities in the load-depth curves.[53] (5) It has been documented that the occurrence of steps during indentation loading of layer minerals affects the resulting Young's modulus.[54] When the recorded load-depth curve does exhibit steps or pop-ins, these discontinuities were removed to reduce h_{max}, thereby obtaining a more accurate Young's modulus.[55] The corrected curves are shown in Fig. 8d. Upon completion of the correction, the PDF deconvolution results of the extracted dataset of nanoindentation on biotite were reassembled and are summarized in Fig. 8b. The peak value of the fitting curve indicates that the Young's modulus of biotite is 49.85 GPa. Additionally, the standard deviation for calculating Young's modulus is 10.07 GPa, which indicates that the distribution of data is very discrete.

5.2.4. Comparison of quartz, feldspar, and biotite

According to the above experimental results, the three rock-forming minerals exhibit different mechanical responses to permanent penetration, which reflects their differences in crystal structure: (1) The penetration depth and size of the residual indents on different minerals increase from quartz to feldspar and then to biotite. (2) The three minerals are sequentially assigned as quartz, feldspar, and biotite in the order of decreasing Young's modulus. (3) The occurrence of long radial cracks indicates that biotite behaves more like a brittle material under nanoindentation (see Fig. 8e). During indentation on biotite, the cracks initiated at the corners where an instant stress concentration exists, and the energy unable to be stored in the adjacent regime is dissipated by cracking.[56] Meanwhile, quartz and feldspar are ductile at this scale because cracking is not observed in Figs. 6c and 7c.

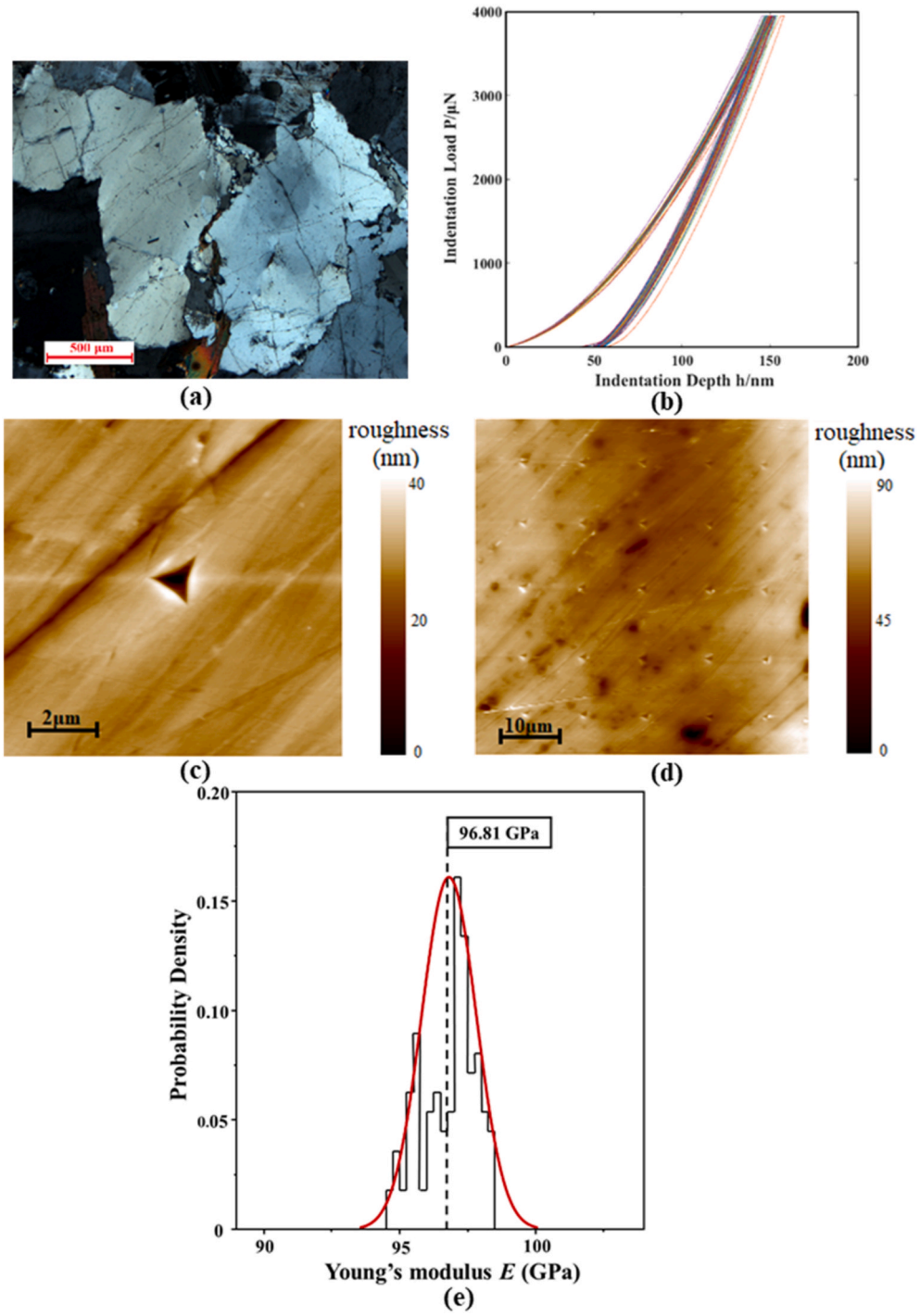


Fig. 6. Results of nanoindentation tests on quartz: (a) perpendicularly polarized light image; (b) load-depth curves; (c) residual indent on quartz; (d) representative SPM image with the size of 60 μm × 60 μm, containing 5 × 5 indent array; (e) frequency plot of grid indentation data.

5.3. Elastic properties of interphases

Crystalline rocks comprise mostly igneous rock types that possess an interlocked structure. Although geologists have conducted extensive studies on various textures of rocks, few attempts have been made in rock mechanics to quantify the influence of contact boundaries on the engineering and mechanical properties of rocks. Noferesti and Rao[57] studied a large number of average macroscale and microscale Young's moduli of crystalline rocks. The mean value of Young's modulus of the minerals is much larger than that of macro rock. Meanwhile, interphases and interactions between minerals also have a significant impact on the elastic properties of rocks. In the present work, a novel methodology was developed to estimate the Young's modulus of interphases based on the experimental results of AFM.

The roughness surface between contact minerals (feldspar-biotite, quartz-biotite, and quartz-feldspar interphases) is presented in Fig. 9. The striped interphases can be easily recognized between two different rock-forming minerals. The shapes of interphases (mineral contact zone) are complex and are gaps with the incursion of their neighboring rock-forming minerals.

The mechanical properties of the intergrowth boundaries between basic minerals composing the Bukit Timah granite are our focus. Fig. 9

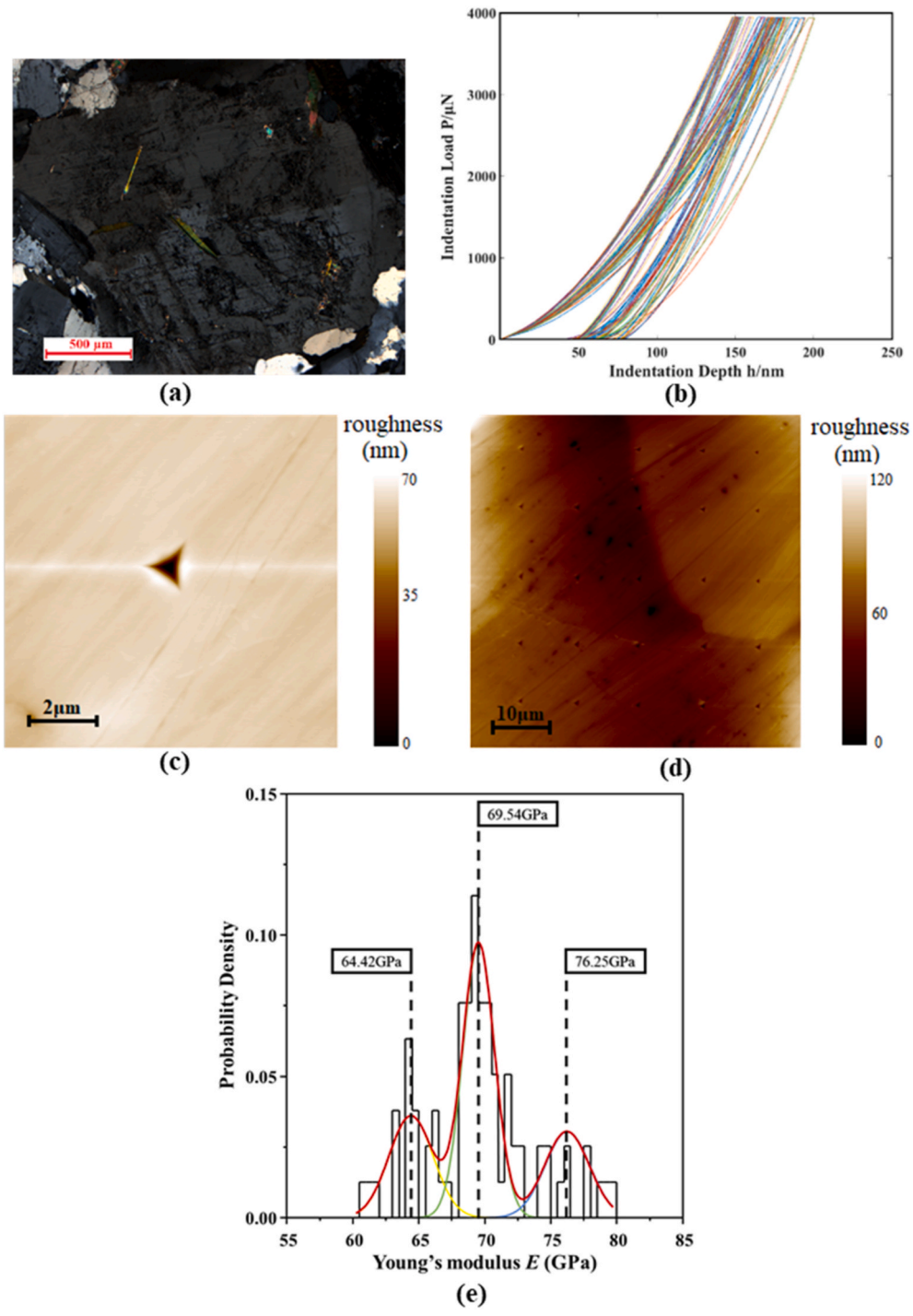


Fig. 7. Results of nanoindentation tests on feldspar: (a) perpendicularly polarized light image; (b) load-depth curves; (c) residual indent; (d) representative SPM image with size of 60 μm × 60 μm containing 5 × 5 indent array; (e) frequency plot of grid indentation data.

illustrates the mechanical property mapping of the interfacial regions of the different phases by AFM. The domain of striped interphases was selected empirically according to the distribution of surface roughness and elastic properties around the interphases. The Young's modulus of interphases was determined by the statistical average of a large number of experimental data in the striped interphase zone. Young's modulus of the quartz-biotite, feldspar-biotite, and quartz-feldspar interphases is 25.15 GPa, 21.39 GPa, and 26.90 GPa, respectively. All are lower than the elastic properties of rock-forming minerals. The average modulus of the interphases is 24.48 GPa, which was used in the following AGBM in section 6.

6. Calculating macroscale elastic property of granitic rocks using AGBM

6.1. Generating numerical models

In this section, an accurate grain-based numerical model of granite was generated based on the microstructure and mechanical properties derived from micro-RME to evaluate the elastic property of granite. AGBM further investigated the influence of the microstructure and mechanical properties of minerals on the macroscale properties of rock samples.

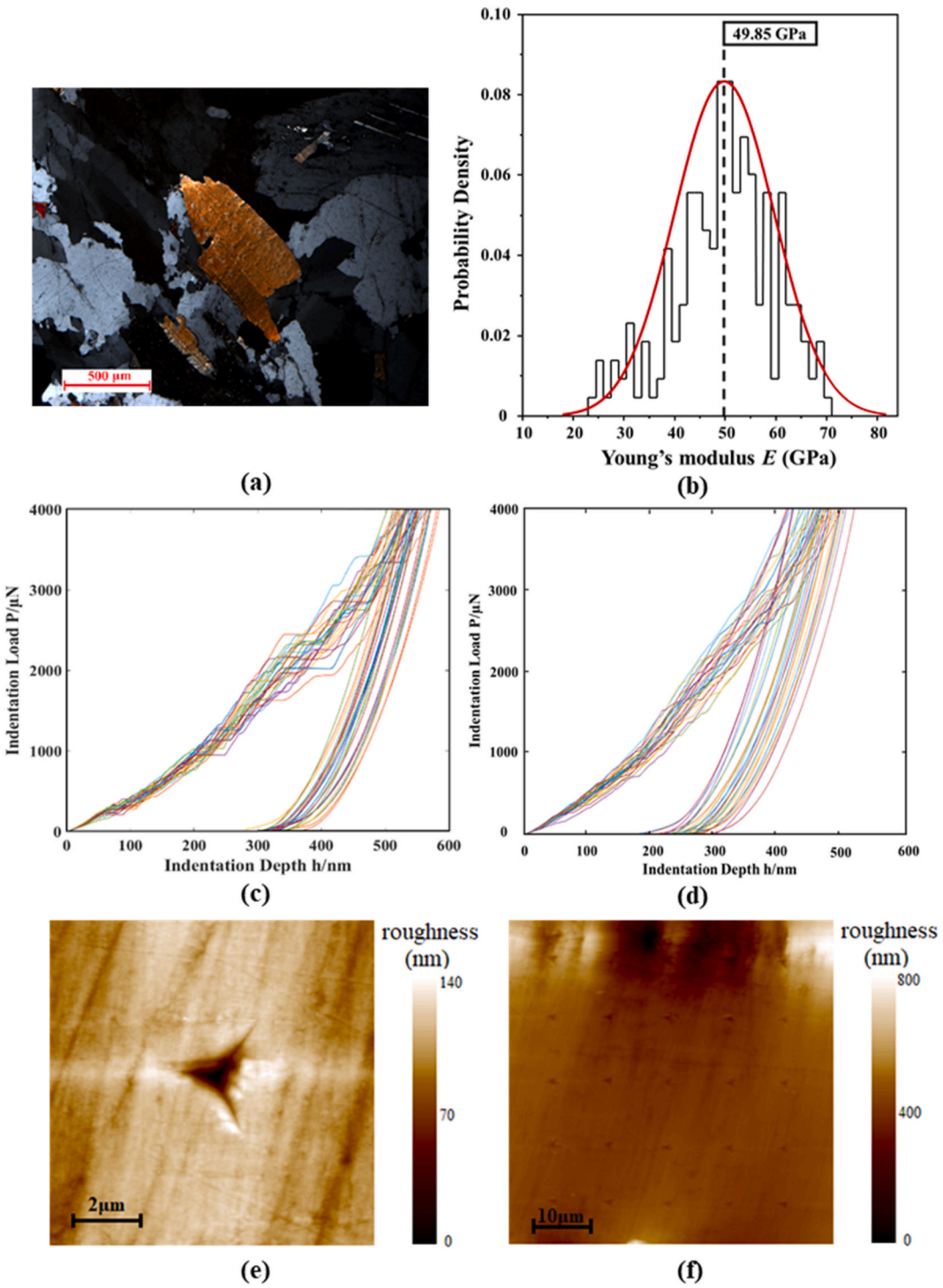


Fig. 8. Results of nanoindentation tests on biotite: (a) perpendicularly polarized light image; (b) frequency plot of grid indentation data; (c) original load-depth curves; (d) corrected load-depth curves; (e) residual indent; (f) representative SPM image with size of 60 μm × 60 μm containing 5 × 5 indent array for biotite.

The digital images obtained by TIMA were transformed into computational numerical models. As stated in section 5.1, an image retrieved from fresh cross sections of rock samples by TIMA can truly reflect the geometrical distribution of different minerals by different gray values. By analyzing the gray values of the image pixels, quartz, feldspar, and biotite grains can be distinguished according to segmentation intervals of 0–85, 86–170, and 171–255, respectively. The pixel representations of the different minerals were mapped to the rectangular elements of the finite element models to characterize the mesostructure based on the image analysis technique. Therefore, accurate grain-based numerical models are exact in terms of (1) mineral volume fraction, (2) mineral morphology, (3) occlusal morphology between minerals, (4) mineral size, and (5) the ratio of maximum to minimum mineral size.

For the simulation of the uniaxial compression of granite to obtain a stress-strain relationship, a numerical model of the granite specimen was established in which both the morphologies and the properties of minerals were taken into account. A computational model with a height of 20 mm and width of 10 mm (Fig. 10a) was cut from Fig. 5. As shown in Fig. 10b, the computational domain of the accurate grain-based numerical model was discretized to 166,753 rectangular finite element

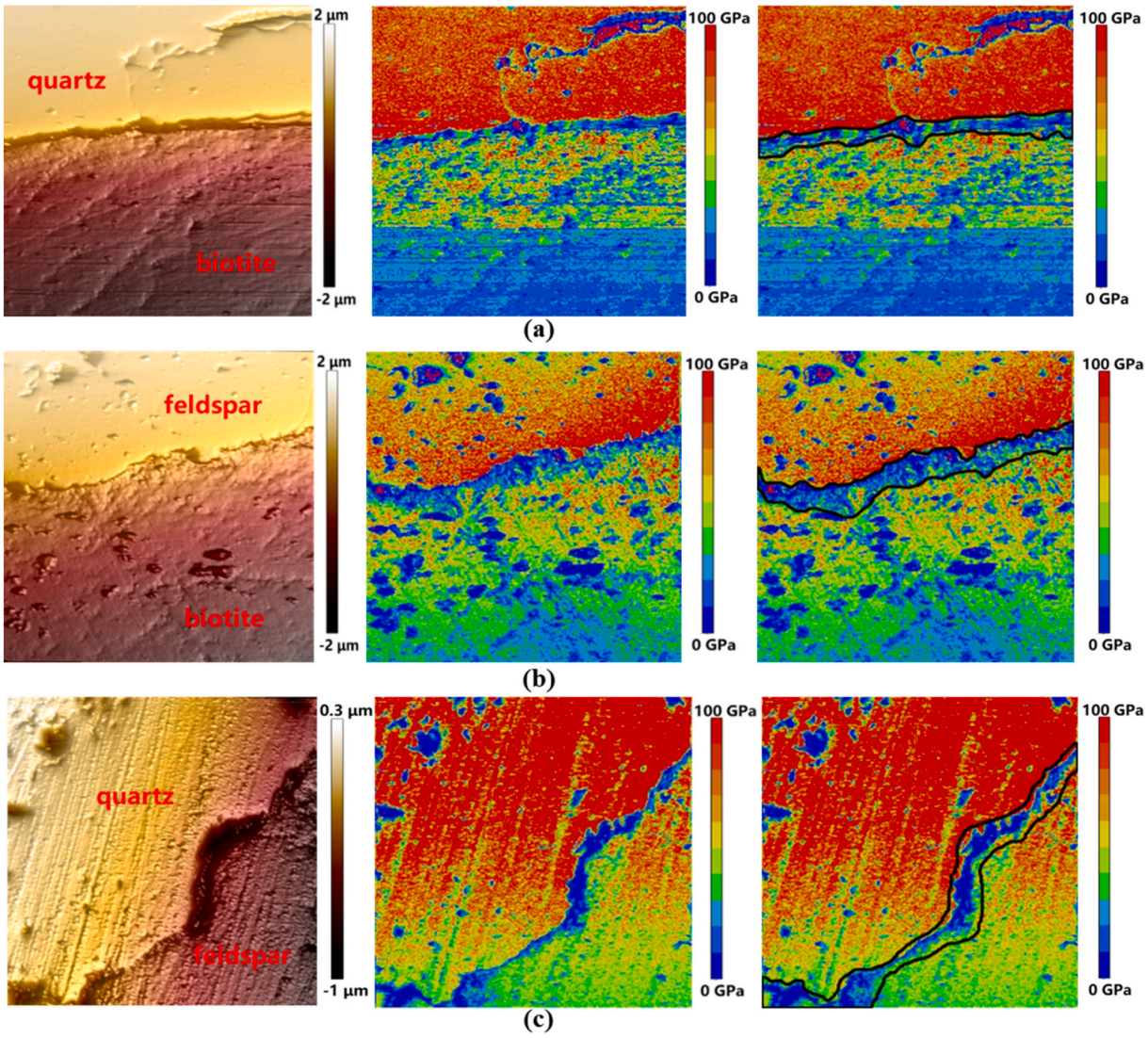


Fig. 9. Surface roughness, elastic property, and striped interphase zone of sample around interphase between (a) quartz and biotite (b) feldspar and biotite, and (c) quartz and feldspar.

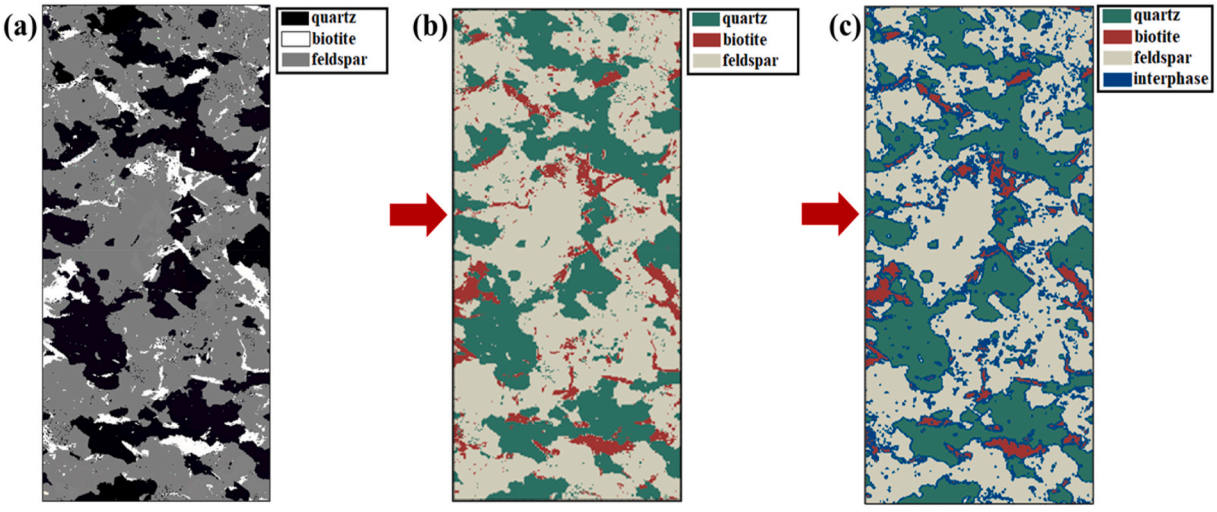


Fig. 10. Generation of accurate grain-based numerical model: (a) TIMA images; (b) set material properties of quartz, feldspar, and biotite-elements using results of nanoindentation test; (c) insert interphase-elements and set their material properties using results of AFM test.

elements.[58–60] The mineral type of elements was determined based on the gray value of the pixel corresponding to the spatial position.

The material properties of mineral grains were assigned according to the set of mineral elements established in the process of mesostructure characterization. The mechanical properties of quartz, feldspar, and biotite elements in the numerical models were determined using the results of the nanoindentation test (see Fig. 10b). The values of other microscale parameters including density and Poisson's ratio of rock-forming minerals were chosen according to the mineral properties suggested by.[4] Quartz and feldspar have similar densities, while the density of biotite is higher. Then, a set of interphase elements was inserted into the numerical models along the boundary of rock-forming minerals (see Fig. 10c). The material properties of all interphase elements between different minerals were assumed to be identical and were set as the results of the AFM tests. All microparameters used in the numerical modeling are listed in Table 3.

6.2. Solving macroscale elastic property using uniaxial compression modeling

This computational model was assumed to be plane strain. A vertical displacement of 0.2 mm was directly imposed on the upper boundary of the computational model, and a vertical constraint was applied on its bottom boundary. To reduce the influence of the end effect during the simulations, the upper and lower steel platens of the model were removed. A time step of 5×10^{-5} ms was chosen to ensure the numerical stability for the explicit time integration scheme.

Because an accurate grain-based numerical model was established based on the real microstructure and microscale mechanical properties, the essential internal relationship between the macroscopic and microscopic mechanical properties can be established directly using AGBM, with the quantitative visualization of interior stress evolution. The stress evolution of the AGBM during the uniaxial compression test is shown in Fig. 11. First, as shown in Fig. 11b and d, the feldspar elements and quartz elements constituted most of the load-bearing capacity and thus experienced higher vertical compressive stress. The compressive stresses within quartz and feldspar, which are mechanically strong, are much higher than the stresses within biotite and interphases, which are mechanically weak. Second, Fig. 11a illustrates that the horizontal tensile stress appears mainly within the feldspar elements and quartz elements, while the horizontal compressive stress is mainly found within biotite elements and interphase elements (especially along the quartz edge). Third, the grains are physically connected, and they cannot deform independently. The stress redistribution is mainly triggered by the different elastic responses of the three rock-forming minerals in granites. The concentration of shear stress is more prevalent when the elastic mismatch between minerals is higher, especially at the boundaries between feldspar and quartz, as depicted in Fig. 11c. The microscale heterogeneity should be considered in order to accurately predict the elastic property and reveal the underlying mechanisms of the failure to be further studied in future work.

As shown in Fig. 12, a stress-strain curve was achieved by the simulation of the uniaxial compression test based on AGBM (see the blue line in Fig. 12). This stress-strain curve shows the relationship between vertical stress and vertical strain, where the slope of this curve represents the macroscale Young's modulus of the rock sample, and the computed value of Young's modulus is 41.78 GPa. The existing result of macro-RME was given by Wong and Maruvanchery,[47] as shown in Fig. 12 and indicated by a red line. Young's modulus obtained by macro-RME experiments is 39.90 GPa. The numerical results of the micro-RME-based models agree well with the results of macro-RME.

Table 3
Material parameters used in accurate grain-based numerical models.

Mineral	Density (kg/m^3)	Young's modulus E (GPa)	Poisson's ratio
Quartz	2650	96.81	0.08
Feldspar	2600	69.50	0.27
Biotite	2850	49.85	0.25
Interphase	2650	24.48	0.23

6.3. Sensitivity analysis for mechanical parameters of interphases

Three computational models with different interphase elastic properties were established to discuss the influence of the interphase mechanical parameters. Assuming that the Young's modulus of the interphases was 78.34 GPa, 49.85 GPa (corresponding to the average value of three rock-forming minerals and Young's modulus of biotite), or the elastic property of interphases was ignored, a set of stress-strain curves was obtained, as shown in Fig. 12. According to the stress-strain curves, Young's modulus of the granite sample was calculated to be 83.37 GPa, 61.60 GPa, and 76.42 GPa, respectively, which are much higher than the results of the macroscopic rock mechanical test. The above results demonstrate that the Young's modulus of granite depends significantly on the elastic modulus of the interphase. It is critical to measure the mechanical property of interphases between different minerals for establishing accurate grain-based numerical models and determining an accurate macroscale Young's modulus of granitic rock.

7. Discussion

Bukit Timah granite with low volumetric porosity was investigated in this work. When the present method is extended to other types of rocks such as sandstone and weathered granite, the following issues should be addressed:

(1) Effect of microcracks and microvoids

It is known that the Young's modulus of rocks decreases with increasing numbers of microcracks and microvoids.[61,62] In this work, the microstructure of samples was measured using the X-ray computed tomography (CT) technique and three-dimensional (3D) image reconstruction. CT scanning was performed on a YXLON FF35 CT (Germany) at a resolution of 10 μm. As shown in Fig. 13, a cubic zone 20 mm × 20 mm × 20 mm in size was chosen, and the black frame represents the analysis area. In the reconstruction images, the colored region represents the microcracks and microvoids. The volumetric porosity (defined as the percentage ratio of the number of volumetric pore voxels to the number of total volumetric voxels) is 1.85%, which means that the porosity of the samples is low. Therefore, the effect of microcracks and microvoids was reasonably ignored in this work. Additionally, the results of TIMA, as shown in Fig. 5, indicate that the present granite sample has low porosity. In future work, the effect of microcracks and microvoids will be further investigated to extend the present work to porous rocks such as sandstones and weathered granite.

(2) Effect of mineral anisotropy

The full elastic tensors of minerals determined by impulse stimulated light scattering[63] and nanoindentation techniques[53] confirm that some minerals exhibit extreme elastic anisotropy. In this work, to reduce the effect of mineral anisotropy, 100 indents were conducted on different regions of each rock-forming mineral during nanoindentation test. Then, the expectancy values of these indenters were calculated for each rock-forming mineral (quartz, feldspar, and biotite) by mathematical statistical methods. In future work, the electron backscatter diffraction (EBSD) technique can be used to investigate the effects of crystallographic preferred orientation (CPO) and shape preferred orientation (SPO).[6]

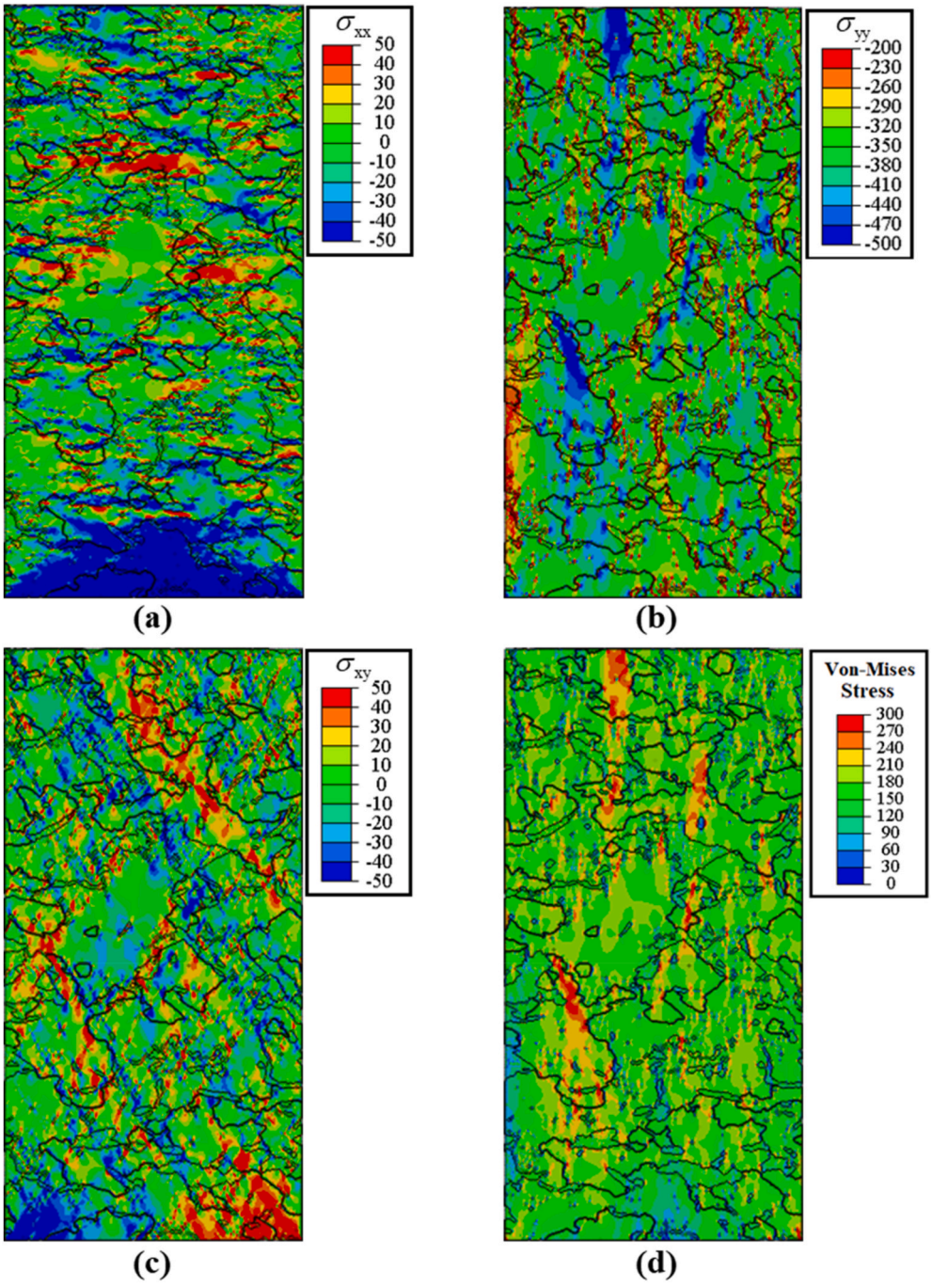


Fig. 11. Simulated results of AGBM under uniaxial compression tests, plotted with boundary of minerals: (a) horizontal stress σ_{xx}; (b) vertical stress σ_{yy}; (c) shear stress σ_{xy}; (d) Von-Mises stress (Unit: MPa).

8. Conclusions

To overcome the challenges of drilling and sampling intact and standard-sized rock samples, we proposed a novel methodology to determine the elastic properties of natural granitic rocks that can be arbitrarily sized and shaped. By conducting micro-RME, the spatial distribution and mechanical properties of rock constituent phases were characterized. With accurate microstructure and micromechanical parameters, AGBM was then developed to derive the macroscale Young's modulus of granite. The following conclusions can be drawn:

(1) The distribution and Young's modulus of rock-forming minerals were measured using TIMA and nanoindentation test, which provided precise microscale parameters for numerical modeling. The different behaviors of the three minerals under nanoindentation reflected their crystal structure and elastic property, while the delamination of biotite indicated that it is a nanostructured layered material.

(2) The morphology and mechanical properties of interphases between different rock-forming minerals were first achieved by AFM test, and the effect of interphases was considered in the numerical model. A sensitivity analysis with numerical results illustrated that interphases have a significant impact on the macromechanical behavior of granites. Without considering interphases, the macroscale elastic property achieved by grain-based modeling was overestimated.

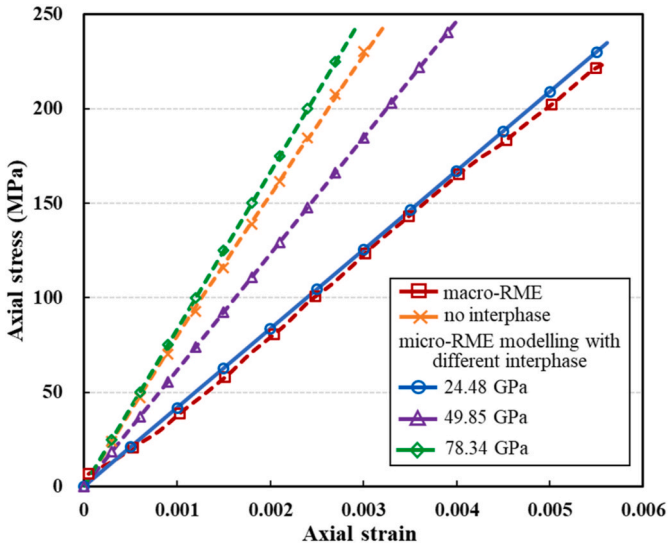


Fig. 12. Comparison between stress-strain curves obtained by existing results of macro-RME (red line) and our results of micro-RME based modeling. (For interpretation of the references to color in this figure legend, the reader is referred to the Web version of this article.)

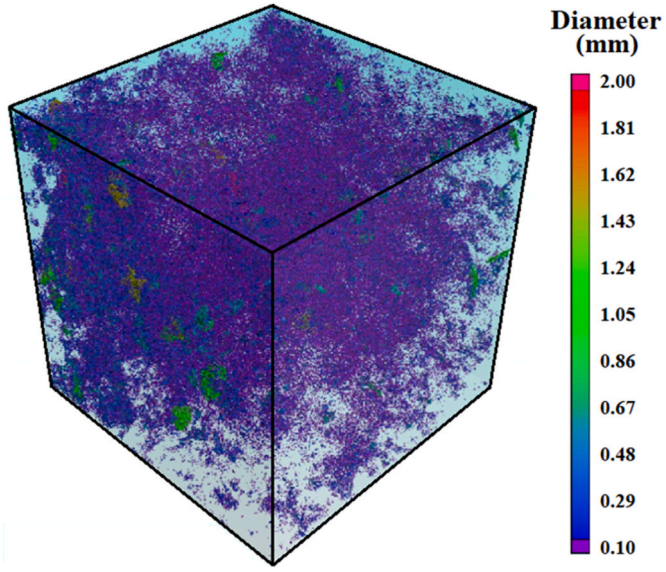


Fig. 13. Pore structures of granite obtained by CT technology.

(3) Accurate grain-based models can be generated using the micro-structure and micromechanical properties achieved by micro-RME. The proposed method provides an innovative tool for investigating the cross-scale elasticity of rock with highly heterogeneous multiphase composites.

Data availability

Datasets related to this article are made available by Zenodo, a public repository of research data, at the following link: https://zenodo.org/record/5729120.

Declaration of competing interest

The authors declare that they have no known competing financial interests or personal relationships that could have appeared to influence the work reported in this paper.

Acknowledgments

This work was supported by the National Natural Science Foundation of China (grant nos. 12172264 and 41941018) and Basic Research Program of Central Government Funds for Shenzhen Science and Technology Development (2021Szvup103).

References

1 Shao Z, Wang Y, Tang X. The influences of heating and uniaxial loading on granite subjected to liquid nitrogen cooling. *Eng Geol*. 2020;271, 105614. https://doi.org/10.1016/j.enggeo.2020.105614.
2 Zhong S, Jiang Q, Liu C, et al. In-site core disking phenomenon and break mechanism of hard marble: investigation in 2400 m deep-buried underground laboratory. *J Cent South Univ*. 2020;27:2959–2970. https://doi.org/10.1007/s11771-020-4521-9.
3 Wang H, Li HB, Zhang L, et al. Paleoseismic slip records and uplift of the Longmen Shan, Eastern Tibetan plateau. *Tectonics*. 2019;38:354–373. https://doi.org/10.1029/2018TC005278.
4 Bass D. Elasticity of minerals, glasses, and melts. In: Ahrens TJ, ed. *Mineral Physics & Crystallography: A Handbook of Physical Constants*. Washington, D. C: American Geophysical Union; 1995:45–63.
5 Hill R. The elastic behavior of a crystalline aggregate. *Proc Phys Soc*. 1952;5: 349–354. https://doi.org/10.1088/0370-1298/65/5/307.
6 Zhong X, Frehner M, Kunze K, Zappone A. A novel EBSD-based finite-element wave propagation model for investigating seismic anisotropy: application to Finero Peridotite, Ivrea-Verbano zone, northern Italy. *Geophys Res Lett*. 2014;41:7105–7114. https://doi.org/10.1002/2014GL060490.
7 Sone H, Zoback MD. Mechanical properties of shale-gas reservoir rocks - part I: static and dynamic elastic properties and anisotropy. *Geophysics*. 2013;78:D378–D389. https://doi.org/10.1190/GEO2013-0050.1.
8 Eshelby J. The determination of the elastic field of an ellipsoidal inclusion, and related problems. *Math Phys Eng Sci*. 1957:376–396. https://doi.org/10.1098/rspa.1957. 0133.
9 Withers P, Stobb W, Pedersen O. The application of the Eshelby method of internal stress determination to short fiber metal matrix composites. *Acta Metall*. 1989: 3061–3084. https://doi.org/10.1016/0001-6160(89)90341-6.
10 Hill R. A self-consistent mechanics of composite materials. *J Mech Phys Solid*. 1965: 213–222. https://doi.org/10.1016/0022-5096(65)90010-4.
11 McLaughlin S. Electrostatic potentials at membrane-solution interfaces. *Curr Top Membr Transport*. 1977;9:71–144. https://doi.org/10.1016/S0070-2161(08)60677-2.
12 Mori T, Tanaka K. Average stress in matrix and average elastic energy of materials with misfitting inclusions. *Acta Metall*. 1973:571–574. https://doi.org/10.1016/0001-6160(73)90064-3.
13 Li Y, Luo S, Lu M, et al. Cross-scale characterization of sandstones via statistical nanoindentation: evaluation of data analytics and upscaling models. *Int J Rock Mech Min*. 2021;142, 104738. https://doi.org/10.1016/j.ijrmms.2021.104738.
14 Tang X, Xu J, Zhang Y, et al. Determining the mechanical parameters of asteroid rocks using nwa13618 meteorites and micro-RME. *Rock Soil Mech*. 2022:43. https://doi.org/10.16285/j.rsm.2021.1342 (in Chinese).
15 Bobko C, Ulm F. The nano-mechanical morphology of shale. *Mech Mater*. 2008;40: 318–337. https://doi.org/10.1016/j.mechmat.2007.09.006.
16 Akono A, Kabir P, Shi Z, et al. Modeling CO_2 induced alterations in Mt. Simon sandstone via nanomechanics. *Rock Mech Rock Eng*. 2019;52:1353–1375. https://doi.org/10.1007/s00603-018-1655-2.
17 Zeng Q, Wu Y, Liu Y, Zhang G. Determining the micro-fracture properties of antrim gas shale by an improved micro-indentation method. *J Nat Gas Sci Eng*. 2019;62: 224–235. https://doi.org/10.1016/j.jngse.2018.12.013.
18 Luo S, Lu Y, Wu Y, et al. Cross-scale characterization of the elasticity of shales: statistical nanoindentation and data analytics. *J Mech Phys Solid*. 2020;140. https://doi.org/10.1016/j.jmps. 2020.103945.
19 Lu Y, Li Y, Wu Y, et al. Characterization of shale softening by large volume-based nanoindentation. *Rock Mech Rock Eng*. 2020;53:1393–1409. https://doi.org/10.1007/s00603-019-01981-8.
20 Xu J, Tang X, Wang Z, et al. Investigating the softening of weak interlayers during landslides using nanoindentation experiments and simulations. *Eng Geol*. 2020;277, 105801. https://doi.org/10.1016/j.enggeo.2020.105801.
21 Voltolini M, Rutqvist J, Kneafsey T. Coupling dynamic in situ X-ray micro-imaging and indentation: a novel approach to evaluate micromechanics applied to oil shale. *Fuel*. 2021:300. https://doi.org/10.1016/j.fuel.2021.120987.
22 Smolyakov G, Formosa-Dague C, Severac C, et al. High speed indentation measures by FV, QI and QNM introduce a new understanding of bionanomechanical experiments. *Micron*. 2016;85:8–14. https://doi.org/10.1016/j.micron.2016.03.002.
23 Trtik P, Kaufmann J, Volz U. On the use of peak-force tapping atomic force microscopy for quantification of the local elastic modulus in hardened cement paste. *Cement Concr Res*. 2012;42:215–221. https://doi.org/10.1016/j.cemconres.2011.08.009.
24 Eliyahu M, Emmanuel S, Day-Stirrat RJ, Macaulay CI. Mechanical properties of organic matter in shales mapped at the nanometer scale. *Mar Petrol Geol*. 2015;59: 294–304. https://doi.org/10.1016/j.marpetgeo.2014.09.007.

25 Emmanuel S, Eliyahu M, Day-Stirrat RJ, et al. Impact of thermal maturation on nano-scale elastic properties of organic matter in shales. *Mar Petrol Geol*. 2016;70:175–184. https://doi.org/10.1016/j.marpetgeo.2015.12.001.

26 Liu Y, Xiong Y, Li Y, Peng P. Effect of thermal maturation on chemical structure and nanomechanical properties of solid bitumen. *Mar Petrol Geol*. 2018;92:780–793. https://doi.org/10.1016/j.marpetgeo.2017.12.008.

27 Liu Y, Sokolov I, Dokukin ME, et al. Can AFM be used to measure absolute values of young's modulus of nanocomposite materials down to the nanoscale? *Nanoscale*. 2020;12:12432–12443. https://doi.org/10.1039/D0NR02314K.

28 Graham SP, Rouainia M, Aplin AC, et al. Geomechanical characterisation of organic-rich calcareous shale using AFM and nanoindentation. *Rock Mech Rock Eng*. 2021;54:303–320. https://doi.org/10.1007/s00603-020-02261-6.

29 Hoek E, Martin CD. Fracture initiation and propagation in intact rock - a review. *J Rock Mech Geotech Eng*. 2014;6:287–300. https://doi.org/10.1016/j.jrmge.2014.06.001.

30 Zhang Y, Wong LNY. A review of numerical techniques approaching microstructures of crystalline rocks. *Comput Geosci*. 2018;115:167–187. https://doi.org/10.1016/j.cageo.2018.03.012.

31 Lan H, Martin CD, Hu B. Effect of heterogeneity of brittle rock on micromechanical extensile behavior during compression loading. *J Mech Phys: Solid Earth*. 2010;115. https://doi.org/10.1029/2009JB006496.

32 Peng J, Wong LNY, Teh CI, Li Z. Modeling micro-cracking behavior of Bukit Timah granite using grain-based model. *Rock Mech Rock Eng*. 2018;51:135–154. https://doi.org/10.1007/s00603-017-1316-x.

33 Wang X, Cai M. Modeling of brittle rock failure considering inter- and intra-grain contact failures. *Comput Geotech*. 2018;101:224–244. https://doi.org/10.1016/j.compgeo.2018.04.016.

34 Peng J, Wong LNY, Teh CI. Influence of grain size heterogeneity on strength and microcracking behavior of crystalline rocks. *J Mech Phys: Solid Earth*. 2017;122:1054–1073. https://doi.org/10.1002/2016JB013469.

35 Zhou W, Ji X, Ma G, Chen Y. FDEM simulation of rocks with microstructure generated by voronoi grain-based model with particle growth. *Rock Mech Rock Eng*. 2020;53:1909–1921. https://doi.org/10.1007/s00603-019-02014-0.

36 Andrae H, Combaret N, Dvorkin J, et al. Digital rock physics benchmarks-part II: computing effective properties. *Comput Geosci*. 2013;50:33–43. https://doi.org/10.1016/j.cageo.2012. 09.008.

37 Mahabadi OK, Randall NX, Zong Z, Grasselli G. A novel approach for micro-scale characterization and modeling of geomaterials incorporating actual material heterogeneity. *Geophys Res Lett*. 2012;39. https://doi.org/10.1029/2011GL050411.

38 Mahabadi OK, Tatone BSA, Grasselli G. Influence of microscale heterogeneity and microstructure on the tensile behavior of crystalline rocks. *J Mech Phys: Solid Earth*. 2014;119:5324–5341. https://doi.org/10.1002/2014JB011064.

39 Abdelaziz A, Zhao Q, Grasselli G. Grain based modelling of rocks using the combined finite-discrete element method. *Comput Geotech*. 2018;103:73–81. https://doi.org/10.1016/j.compgeo.2018.07. 003.

40 Derjaguin BV, Muller VM, Toporov YP. Effect of contact deformations on the adhesion of particles. *J Colloid Interface Sci*. 1975;2:314–326.

41 Hrstka T, Gottlieb P, Skála R, et al. Automated mineralogy and petrology - applications of Tescan integrated mineral analyzer (TIMA). *J Geosci*. 2018:47–63. https://doi.org/10.3190/jgeosci.250.

42 Harvey PJ, Rouillon M, Dong C, et al. Geochemical sources, forms and phases of soil contamination in an industrial city. *Sci Total Environ*. 2017;584–585:505–514. https://doi.org/10.1016/j.scitotenv. 2017.01.053.

43 Oliver WC, Pharr GM. An improved technique for determining hardness and elastic modulus using load and displacement sensing indentation experiments. *J Mater Res*. 1992;7:1564–1583. https://doi.org/10.1557/JMR.1992.1564.

44 Oliver WC, Pharr GM. Measurement of hardness and elastic modulus by instrumented indetation: advances in understanding and refinements to methodology. *J Mater Res*. 2004;19:3–20. https://doi.org/10.1557/jmr.2004.19.1.3.

45 Constantinides G, Ravi Chandran KS, Ulm FJ, Van Vliet KJ. Grid indentation analysis of composite microstructure and mechanics: principles and validation. *Mater Sci Eng*. 2006;430:189–202. https://doi.org/10.1016/j.msea.2006.05.125.

46 Sneddon IN. The relation between load and penetration in the axisymmetric boussinesq problem for a punch of arbitrary profile. *Int J Eng Sci*. 1965:47–56. https://doi.org/10.1016/0020-7225(65)90019-4.

47 Wong LNY, Maruvanchery V. Different lithological varieties of bukit timah granite in Singapore: a preliminary comparison study on engineering properties. *Rock Mech Rock Eng*. 2016;49:2923–2935. https://doi.org/10.1007/s00603-015-0825-8.

48 Zhao J, Bergh-Christensen J. Construction and utilization of rock caverns in Singapore Part D: two proposed cavern schemes. *Tunn Undergr Space Technol*. 1996;11:85–91. https://doi.org/10.1016/0886-7798(96)00057-0.

49 Zhao J, Lee KW. Construction and utilization of rock caverns in Singapore; Part C, planning and location selection. *Tunn Undergr Space Technol*. 1996;11:81–84. https://doi.org/10.1016/0886-7798(96)00056-9.

50 Cowie S, Walton G. The effect of mineralogical parameters on the mechanical properties of granitic rocks. *Eng Geol*. 2018;240:204–225. https://doi.org/10.1016/j.enggeo.2018.04.021.

51 Viktorov SD, Golovin YI, Kochanov AN, et al. Micro- and nano-indentation approach to strength and deformation characteristics of minerals. *J Min Sci*. 2014;50:652–659. https://doi.org/10.1134/S1062739114040048.

52 Mavko G, Mukerji T, Dvorkin J. *The Rock Physics Handbook: Tools for Seismic Analysis of Porous Media*. New York: Cambridge university; 2003.

53 Pant R, Liming H, Zhang G, et al. *Anisotropy of Mica Probed by Nanoindentation*. Berlin: Springer; 2013:239–245. https://doi.org/10.1007/978-3-642-32492-5_30.

54 Zhang J, Hu L, Pant R, et al. Effects of interlayer interactions on the nanoindentation behavior and hardness of 2:1 phyllosilicates. *Appl Clay Sci*. 2013;80–81:267–280. https://doi.org/10.1016/j.clay.2013.04.013.

55 Zhang G, Wei Z, Ferrell R. Elastic modulus and hardness of muscovite and rectorite determined by nanoindentation. *Appl Clay Sci*. 2009;43:271–281. https://doi.org/10.1016/j.clay.2008.08.010.

56 Chen J. Indentation-based methods to assess fracture toughness for thin coatings. *J Phys D Appl Phys*. 2012;45. https://doi.org/10.1088/0022-3727/45/20/203001.

57 Noferesti H, Rao KS. Role of crystal interlocking on the strength of brittle rocks. *Rock Mech Rock Eng*. 2011;44:221–230. https://doi.org/10.1007/s00603-010-0094-5.

58 Tang X, Rutqvist J, Hu M, Rayudu NM. Modeling three-dimensional fluid-driven propagation of multiple fractures using tough-femm. *Rock Mech Rock Eng*. 2019;52:611–627. https://doi.org/10.1007/s00603-018-1715-7.

59 Zienkiewicz O, Taylor R. *The Finite Element Method*. fifth ed. vol. 1. Oxford: Butterworth-Heinemann; 2000.

60 Tang X, Tao S, Li P, et al. The propagation and interaction of cracks under freeze-thaw cycling in rock-like material. *Int J Rock Mech Min*. 2022;154, 105112. https://doi.org/10.1016/j.ijrmms. 2022.105112.

61 Abe S. Comparison of discrete element simulations to theoretical predictions of the elastic moduli of damaged rocks. *Int J Rock Mech Min*. 2016;88:265–272. https://doi.org/10.1016/j.ijrmms. 2016.07.022.

62 Fakhimi A, Gharahbagh EA. Discrete element analysis of the effect of pore size and pore distribution on the mechanical behavior of rock. *Int J Rock Mech Min*. 2011;48:77–85. https://doi.org/10.1016/j.ijrmms.2010.08.007.

63 Waeselmann N, Brown JM, Angel RJ, et al. The elastic tensor of monoclinic alkali feldspars. *Am Mineral*. 2016;101:1228–1231. https://doi.org/10.2138/am-2016-5583.